Available online at www.sciencedirect.com
ScienceDirect
Acta Materialia 56 (2008) 1274–1287
Acta MATERIALIA
www.elsevier.com/locate/actamat

A framework for automated analysis and simulation of 3D polycrystalline microstructures. Part 2: Synthetic structure generation ☆

Michael Groeber [a,*], Somnath Ghosh [b], Michael D. Uchic [c], Dennis M. Dimiduk [c]

[a] *Graduate Research Associate, Materials Science and Engineering, The Ohio State University, Columbus, OH 43210, USA*
[b] *Nordholt Professor, Mechanical Engineering and Materials Science and Engineering, The Ohio State University, Columbus, OH 43210, USA*
[c] *Air Force Research Laboratory, Materials and Manufacturing Directorate, AFRL/MLLMD, Wright-Patterson AFB, OH 45433, USA*

Received 7 April 2007; received in revised form 11 October 2007; accepted 15 November 2007
Available online 5 February 2008

Abstract

This is the second of a two-part paper intended to develop a framework for collecting data, quantifying characteristics and subsequently representing microstructural information from polycrystalline materials. The framework is motivated by the need for incorporating accurate three-dimensional grain-level morphology and crystallography in computational analysis models that are currently gaining momentum. Following the quantification of microstructural features in the first part, this paper focuses on the development of models and codes for generating statistically equivalent synthetic microstructures. With input in the form of statistical characterization data obtained from serial-sectioning of the microstructures, this module is intended to provide computational modeling efforts with a microstructure representation that is statistically similar to the actual polycrystalline material.
Published by Elsevier Ltd on behalf of Acta Materialia Inc.

Keywords: Serial-sectioning; Electron backscattering diffraction (EBSD); Crystal structure; Modeling

1. Introduction and scope of Part 2

Historical studies have established the knowledge that the size, shape, orientation and spatial arrangement of grains can have a significant influence on the mechanical properties of materials, especially extreme properties like fracture toughness, ductility and fatigue life. Morphological and crystallographic characteristics of microstructure, alongside other variables like loading conditions, part geometry and grain-level constitutive properties, are among the most important parameters in behavioral prediction. Thus, the ability to represent microstructure with high fidelity in computational models is vital to their capability of making accurate property predictions. Classical methods of microstructure representation have included the use of simple geometric features like cubes, spheres and ellipsoids [1–3]. These simple shapes often grossly misrepresent the true grain structure. Other studies have employed tessellation techniques to generate 3D microstructures [4–7]. Tessellated structures have been shown to quantitatively match some microstructural statistics in a better way, especially in comparison with those created

☆ This two-part paper outlines a methodology for automated 3D characterization and representation of polycrystalline microstructures. The first part of the paper-set focuses on techniques used to analyze and quantify data collected during a serial-sectioning experiment, which has been presented in previous papers. The second part gives a detailed description of the application of the analysis to synthetic structure generation. This paper-set is meant to serve as an introduction to a framework for 3D characterization and representation of microstructure. The ultimate goal of this work is to supply computational modeling efforts with realistic microstructure inputs.

* Corresponding author. Tel.: +1 614 203 1403.
E-mail addresses: groeber.9@osu.edu (M. Groeber), ghosh.5@osu.edu (S. Ghosh), Michael.Uchic@wpafb.af.mil (M.D. Uchic), Dennis.Dimiduk@wpafb.af.mil (D.M. Dimiduk).

1359-6454/$34.00 Published by Elsevier Ltd on behalf of Acta Materialia Inc.
doi:10.1016/j.actamat.2007.11.040

by the simple geometric models [4]. However, for tessellations based on randomly dispersed seed or generating points, higher-order moments of certain parameter distributions could deviate significantly from experimental values [6]. To correct for these aberrations, some tessellation methods have incorporated limited data from 2D statistical analyses based on surface data obtained from experiments [7]. However, in general, 2D statistics are insufficient to predict the true 3D characteristics, unless coupled with stereological methods [8]. The current state-of-the-art stereological methods are generally limited to lower-order moments of microstructural parameter distributions and are not adept at predicting the higher-order moments. Further, some aspects of microstructure cannot be inferred at all from 2D sections [9].

The present work is an attempt to develop a robust framework for simulating 3D microstructural models using an integrated experimental–computational approach. The generation process, by assembling a sequence of modules, produces simulated microstructures termed statistically induced realistic instantiations (SIRIs). This paper discusses the essential steps in the generation of SIRIs to represent or simulate microstructures from the serial-sectioning data presented in Part 1 of this paper. The SIRI generation methodology is made up of four principal modules to complete the major steps of the process, which are as follows: equivalent ellipsoidal grain generator, constrained grain packer, seed point generator-constrained Voronoi tessellation tool and crystallographic orientation assignment. Fig. 1 provides a flow diagram of the modules accompanied by their governing principles, objectives and required inputs. The collection of these algorithms or modules and the experimental characterization processes define a new and automated methodology for providing a more complete description and representation of grain-level microstructures.

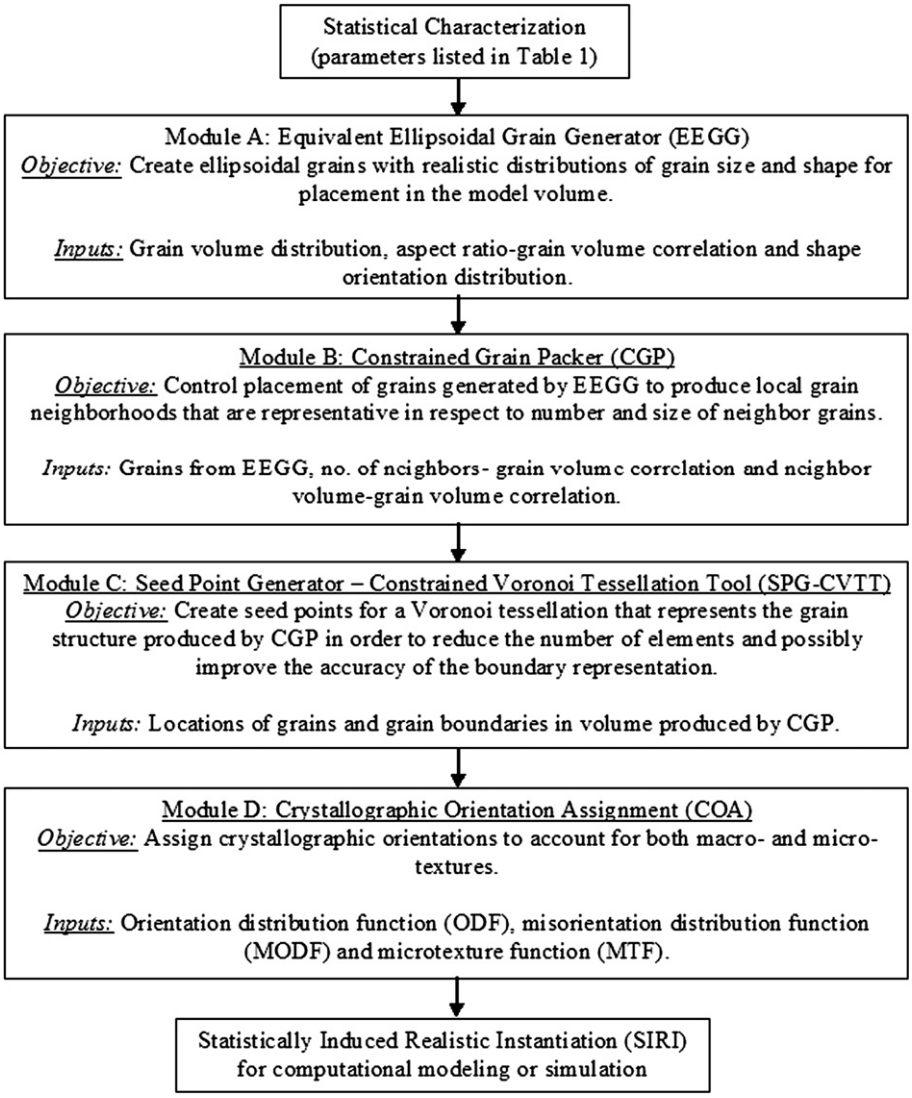

Fig. 1. Flow diagram of the SIRI generation process. The governing principles, objectives and required inputs for each module are listed.

2. Development of algorithms and modules for the SIRI generation process

The statistically equivalent microstructure simulation algorithm starts with a synthesis of the set of statistical descriptors presented in Part 1. This task classifies the statistical descriptors into two distinct categories, viz. (a) those used to provide input conditions and constraints in the microstructure generation process, and (b) those used as validation metrics. Table 1 lists the entire suite of descriptors available and identifies their classification. The following algorithms and modules are developed in sequence to construct the synthetic microstructure simulation process.

2.1. Module A: Equivalent ellipsoidal grain generator (EEGG)

The equivalent ellipsoidal grain generator (EEGG) module is responsible for the creation of a collection of idealized ellipsoidal grains having distributions of size, shape and shape orientation equivalent to those observed in the experimental volume. In this representation, each grain is modeled as an ellipsoid as defined in Part 1. The size corresponds to the volume of each ellipsoid, the shape corresponds to the aspect ratios of the principal axes (b/a, c/a and c/b) and the shape orientation corresponds to the orientation of the major principal axis (a:$a \geqslant b \geqslant c$) relative to the global coordinates. The first step in the process is to sample the experimental grain volume distribution, which is represented by the cumulative probability distribution function (CPDF) fit to the experimental data. In Part 1, the grain volume distribution was shown to be best represented by a log-normal distribution, whose CPDF is given by

$$P(V) = \begin{cases} \frac{1}{2}\left(1 - \operatorname{erf}\left(\frac{V_g^{AVG} - V}{V_g^{STD}\sqrt{2}}\right)\right) \rightarrow V < V_g^{AVG}, \\ \frac{1}{2}\left(1 + \operatorname{erf}\left(\frac{V - V_g^{AVG}}{V_g^{STD}\sqrt{2}}\right)\right) \rightarrow V > V_g^{AVG}. \end{cases} \quad (1)$$

Here, V is the grain volume, $P(V)$ is its cumulative probability, which has 0 and 1 as its limits. The average grain volume (V_g^{AVG}) and the standard deviation (V_g^{STD}) are parameters that determine the precise shape of the distribution function. During ellipsoidal grain volume assignment, a number within the limits of $P(V)$ is randomly generated and the corresponding grain volume, given by Eq. (1), is assigned. This assignment process is continued until the total volume of all grains generated equals a threshold defined as 110% of the volume of the synthetic microstructural model. The additional 10% is needed because some grains may lie partially outside the domain of the microstructural model. This issue will be discussed further in the next subsection.

Subsequent to the grain volume assignment, grain shapes are assigned in conformity with CPDFs of the ellipsoid aspect ratios (b/a, c/a and c/b) that have been established a priori from the experimental data. The corresponding CPDFs can be represented in terms of a beta distribution, with the form:

$$P(b/a) = \frac{\int_0^{b/a} t^{p-1}(1-t)^{q-1}\mathrm{d}t}{B(p,q)}, \quad 0 \leqslant b/a \leqslant 1. \quad (2)$$

In Eq. (2), $B(p,q) = \int_0^1 t^{p-1}(1-t)^{q-1}\mathrm{d}t$ is the beta function, p and q are the shape parameters and $P(b/a)$ is the cumulative probability. Part 1 has established the correlation between the shape and the size of each grain, represented by the aspect ratios and volume of each ellipsoid. To establish this correlation for the synthetic ellipsoidal grains, each volume is converted to an equivalent sphere diameter (ESD) using the relation:

Table 1
List of statistical descriptors measured during the characterization presented in the first paper

Descriptor 1	Descriptor 2	Descriptor type	Classification
Grain volume	N/A	Morphological	Input condition
Spatial orientation	N/A	Morphological	Input condition
Orientation distribution function	N/A	Crystallographic	Input condition
Misorientation distribution function	N/A	Crystallographic	Input condition
Microtexture function	N/A	Crystallographic	Input condition
Number of contiguous neighbors	Grain volume	Correlation	Input condition
Contiguous neighbor size	Grain volume	Correlation	Input condition
Aspect ratio 1 (b/a)	Grain volume	Correlation	Input condition
Aspect ratio 2 (c/a)	Grain volume	Correlation	Input condition
Aspect ratio 3 (c/b)	Grain volume	Correlation	Input condition
Number of contiguous neighbors	N/A	Morphological	Validation metric
Aspect ratio 1 (b/a)	N/A	Morphological	Validation metric
Aspect ratio 2 (c/a)	N/A	Morphological	Validation metric
Aspect ratio 3 (c/b)	N/A	Morphological	Validation metric
Surface-to-volume ratio	N/A	Morphological	Validation metric
Ellipsoidal misfit	N/A	Morphological	Validation metric
Surface-to-volume ratio	Grain volume	Correlation	Validation metric
Ellipsoidal misfit	Grain volume	Correlation	Validation metric

Some descriptors are directly used in constraining the synthetic structure generation process, while others are used only to compare the two structures.

$$\mathrm{ESD} = 2 \cdot \left(\frac{3}{4\pi} V\right)^{\frac{1}{3}}. \quad (3)$$

As discussed in Part 1, the correlation is determined by assigning aspect ratios to different volumetric bins that are represented by ranges of ESD values. The two aspect ratios that define an ellipsoid (b/a and c/a) each have a CPDF in every volume bin. The sampling of the b/a and c/a CPDFs is identical to that of the grain volume CPDF. This process ensures appropriate correlation between the shape and size distributions.

In addition to a correlation with grain volume, the aspect ratios b/a and c/a should also be mutually correlated. However, there was an insufficient number of grains in the serial-sectioning experiment conducted in Part 1 to determine this correlation table between the grain volume V, and both of the aspect ratios b/a and c/a. To overcome this shortcoming, individual correlation functions are generated between V and each of the aspect ratios separately. In this process, values of b/a and c/a are evaluated corresponding to randomly chosen $P(\frac{b}{a})$ and $P(\frac{c}{a})$ values from the $P(\frac{b}{a})$–$(\frac{b}{a})$ and $P(\frac{c}{a})$–$(\frac{c}{a})$ plots, respectively. The consequent aspect ratio $\frac{c}{b} = \frac{c}{a} \div \frac{b}{a}$ is evaluated and its probability density

$$p(c/b) = \frac{(c/b)^{p-1} \cdot (1 - c/b)^{q-1}}{B(p,q)}, \quad 0 \leqslant c/b \leqslant 1$$

is ascertained from the experimentally observed distribution. The two individually generated aspect ratios are accepted with the same probability density of $p(c/b)$.

The third variable, the shape orientation of each ellipsoidal grain, is defined by a set of rotations (θ, λ, ψ) needed to transform the global coordinates (X, Y, Z) onto the principal axes of the ellipsoid (A, B, C). The probability density function, $f(g)\Delta g = \frac{\Delta N_g}{N}$ is the probability of observing an orientation G in the interval $g \leqslant G \leqslant g + \Delta g$, where ΔN_g is the number of orientations between g and $g + \Delta g$ and N is the total number of experimentally observed ellipsoidal grains. If $N^{(i)}$ is the number of points in the ith orientation space element ranging from (θ, λ, ψ) and $(\theta + \Delta\theta, \lambda + \Delta\lambda, \psi + \Delta\psi)$, then the density of orientations can be expressed as $\frac{N^{(i)}}{N}$. To evaluate this density, the entire orientation space is defined as a finite cube with edge length π (180°) with the origin at one of its vertices. For the purpose of creating ranges in the orientation data, the orientation space is discretized into cubic bins of dimension $\pi/36$ or 5°. The shape orientation density in each bin is calculated by dividing the number of orientations in the bin by the total number of orientations in the experimental data. Ellipsoidal shape orientations are created and assigned based on this probability density function.

In summary, the output of this module is a set of representative ellipsoidal grains having statistically equivalent volumes, aspect ratios and shape orientations as the experimental reference data. However, this module does not arrange the grains in their appropriate spatial locations, which is the function of the next module.

2.2. Module B: Constrained grain packer (CGP)

This module focuses on the placement of the grains generated by the EEGG module inside of a representative volume. For this study, the representative volume is selected to be nominally the same dimensions as the experimental volume. The effect of dramatically changing the dimensions of the representative volume has not been investigated and is the focus of ongoing studies. The CGP module utilizes a number of constraints to determine the arrangement and spatial location of the grains inside this model volume. Two correlation functions (listed in Table 1) are used in the grain placement process. They are: (i) the correlation between the number of contiguous grains and the grain volume, and (ii) the correlation between the distribution of contiguous grain sizes and the grain volume. As a first step, the CGP module discretizes the representative volume into a grid of voxels. Ellipsoidal grains, with defined size, shape and shape orientations, are sequentially placed within the representative volume by randomly choosing the position of their centroids. All the voxels that lie within the ellipsoid's boundary are identified as those belonging to this grain. The resulting grain position is checked against a set of constraints to define its acceptability. The following subsections discuss the constraints that are used in this process, as well as the gap filling algorithm that follows grain placement.

2.2.1. Constraint 1: Retention of defined grain volume

The first constraint for grain placement ensures that the majority of voxels that comprise the ellipsoid are unassigned, as a voxel cannot be assigned to multiple grains, and once assigned, is not available for another grain. Specifically, this constraint sets a minimum percentage (R) of voxels within the ellipsoid that must be unassigned, and is expressed as

$$\frac{\sum_{i=0}^{N} \delta_i^1 \delta_i^2}{\sum_{i=0}^{N} \delta_i^1} \times 100 \geqslant R, \quad (4)$$

where N is the total number of voxels and

$$\delta^1 = \begin{cases} 1 \rightarrow \text{inside}, \\ 0 \rightarrow \text{outside}, \end{cases} \quad \text{and} \quad \delta^2 = \begin{cases} 1 \rightarrow \text{unassigned}, \\ 0 \rightarrow \text{assigned}. \end{cases}$$

For positions near the edge of the microstructural model, it is possible for the ellipsoid to extend beyond the boundaries of the representative volume. As a result, a grain may have a significant portion lying outside of the domain of the representative volume. However, as long as a high percentage, e.g. 80%, of the portion inside the volume is unassigned, the requirement imposed by this constraint is satisfied. The 80% value is empirical and has been selected to be a compromise between the rate of ellipsoid placement and the accuracy of initial size. The empirical value also agrees well with the observation that at the end of the grain placement there is generally 15–25% of the representative volume left unassigned. The unassigned volume is allocated

to grains and generally corrects for the allowance of overlap. Allowing the ellipsoids to extend beyond the boundaries of the domain simulates the random sectioning of a volume from a larger sample, where some grains will inevitably intersect the surface of the volume. If the constraint given by Eq. (4) is not satisfied, a new position is selected for the grain.

2.2.2. Constraint 2: Statistical equivalence of number of neighbor grains

The second constraint for grain placement utilizes the correlation function between the number of contiguous neighbors and the grain size. Each grain size bin, corresponding to a range of volumes, has a PDF of the number of contiguous neighboring grains. Each grain previously placed in the representative volume has a given number of neighbors prior to the placement of the grain under consideration. With the addition of the grain under consideration, all of the previously placed and contiguous grains would have an increase in their number of neighbors by one. Constraint 2 examines the total change of probability of the number of neighbors for all the previously placed contiguous grains, and is represented by the inequality:

$$\sum_{i=0}^{N} \left(P_{v(i)}(n+1) - P_{v(i)}(n)\right) \geqslant 0. \tag{5}$$

Here, $P_{v(i)}$ is the probability of the number of neighbors for the volume bin in which the ith grain belongs, N is the number of grains that neighbor the grain under consideration and n is the number of neighbors of a previously placed grain prior to the placement of the grain under consideration. If constraint 2 is satisfied, the overall effect of adding the grain under consideration to the local neighborhood is beneficial; or else a new position is selected.

2.2.3. Constraint 3: Statistical equivalence of size of neighbor grains

The third constraint for grain placement utilizes the correlation function between the distribution of the size of contiguous neighbors and the grain size. Each grain size bin has an experimentally determined PDF of the sizes of the contiguous neighboring grains. Prior to the placement of a grain under consideration, the neighbor size distributions for all previously placed and contiguous grains are calculated. These distributions would change with placement of the grain under consideration. To aid the placement process, an error measure is first defined as the difference between the experimentally determined PDF and the neighbor size distribution prior to the placement of the grain under consideration for each previously placed grain:

$$\mathrm{SE} = \sum_{i=0}^{N_\mathrm{b}} (\mathrm{PDF}_i - \mathrm{CNSD}_i)^2, \tag{6}$$

where N_b is the number of size bins and PDF_i and CNSD_i are the densities of the experimentally determined PDF and neighbor size distribution of the volume bin in which the ith grain belongs, respectively. The error SE is again calculated after placement of the grain under consideration. The change $\Delta\mathrm{SE} = \mathrm{SE}^{\mathrm{after}} - \mathrm{SE}^{\mathrm{before}}$ as a consequence of the new grain placement is summed for all the previously placed grains. For a converging algorithm the sum of ΔSE for each grain should progressively decrease. Hence, the constraint on the change in SE between the experimentally determined PDFs and the neighbor size distributions is given by the inequality:

$$\sum_{i=0}^{N} \Delta\mathrm{SE} \leqslant 0, \tag{7}$$

where N is the number of grains that neighbor the grain under consideration. If this constraint of Eq. (7) is satisfied, the overall affect of adding the grain under consideration to the local neighborhood is beneficial; else a new position is selected.

2.2.4. Constraint 4: Avoid grain containment

The final constraint ensures that no grain is fully contained within another grain. The voxels belonging to each previously placed grain are checked to see if they lie within the grain under consideration. This constraint requires that no contiguous grain can have all of its voxels inside of the grain under consideration. If δ_i corresponds to a relative location indicator where $\delta_i = 1$ if the voxel is contained in the grain under consideration and $\delta_i = 0$ if the voxel is not contained in the grain under consideration, a constraint condition can be developed as

$$\frac{\sum_{i=1}^{N_\mathrm{v}} \delta_i}{N_\mathrm{v}} < 1, \tag{8}$$

where N_v is the number of voxels in the previously placed grain. If the constraint of Eq. (8) is satisfied for each previously placed grain, the grain under consideration is placed; else a new position is selected.

2.2.5. Allocation of unassigned volume to grains

Upon placement of all ellipsoidal grains, there will inevitably be small clusters of unassigned voxels corresponding to morphological incompatibility of the ellipsoidal grains. This operation fills the unassigned regions by a pseudo-grain coarsening process. The coarsening process starts with the determination of which grain shares the most surface area with each of the unassigned voxels. This is done by checking which grains own the six neighbors, corresponding to the six faces, of each unassigned voxel. The unassigned voxels are assigned to the grain with which they share the most surface area. If a voxel shares equal surface area with two grains, the grain whose voxelized volume currently deviates the most from the volume it was assigned by the EEGG module prior to placement and overlaps, accepts the unassigned voxel. That is, when a grain is placed such that it slightly overlaps a previously placed grain, the number of voxels (or volume) belonging to the grain is less than the desired amount. Grains

with larger deviations from their desired amount are given priority when assigning the remaining voxels, but only if there is a tie with respect to the surface area criterion. This process helps to correct for overlaps and ensures that grains are close to their experimentally generated (or desired) volume. A voxel that has no assigned neighbors cannot be assigned to a grain during a coarsening step. The coarsening process continues iteratively until all unassigned voxels have been assigned to grains in the representative polycrystalline volume.

The output of this CGP module is a fully dense, discretized volume filled with representative grains from input provided by the previous EEGG module. The grains are arranged in a manner that produces local grain neighborhoods that are statistically equivalent to the observed experimental neighborhoods. It should be clarified that the grain representations from the CGP module are no longer ellipsoidal. The deviation from the prior ellipsoidal representation is only an effect of allowing overlap during placement of grains and assignment of remaining voxels. The grains remain roughly ellipsoidal in shape; however, they can exhibit local surface undulations. A representative volume with 5269 grains, constructed by the CGP module, is depicted in Fig. 2b along with the experimental volume in Fig. 2a. The corresponding comparison with the experimental statistics is shown in Fig. 4. A discussion of the statistical comparison, in an effort to validate the structure, will be offered in Section 3.

2.3. Module C: Seed point generator-constrained Voronoi tessellation tool (SPG-CVTT)

A finite-element model, in which each voxel is an element, typically leads to a large computational cost. It is often the case that such resolution (or mesh density) is not mandated by the requirements of the solution. Additionally, the user generally does not have control over the mesh density in a voxel-based mesh. In order to avert this computational inefficiency, it is important to completely substitute the voxelized representation of the grain aggregate by a solid-body surface representation, which also removes the discrete voxel faceted nature of the grain surfaces. A representation more consistent with a CAD-based representation offers better control to provide optimal efficiency and accuracy.

One possible approach, developed by the authors in Refs. [10,11], involves smoothing of the grain surfaces through the use of parametric surface representations. However, this process is relatively computationally intensive due to the requirements of robust surface fitting to a large number of data points for grain interfaces. To circumvent this shortcoming, a special tessellation process called the constrained Voronoi tessellation method (CVTM) is employed with an interface to the previously discussed CGP module. Traditional random Voronoi tessellation is based on random seed points, corresponding to the centroids of each Voronoi cell. Details on the definition and construction of Voronoi diagrams can be found in Refs. [12–14]. This process generally does not yield grain topologies consistent with experimental observations. For example, it has been shown in Ref. [13] that the average number of neighboring cells in a random Voronoi tessellation is approximately 15.5. However, as seen in Part 1 the same statistic for IN100 is 12.9. Also, the random Voronoi tessellation process leads to a normal distribution of cell size [13]. This is in significant deviation from the log-nor-

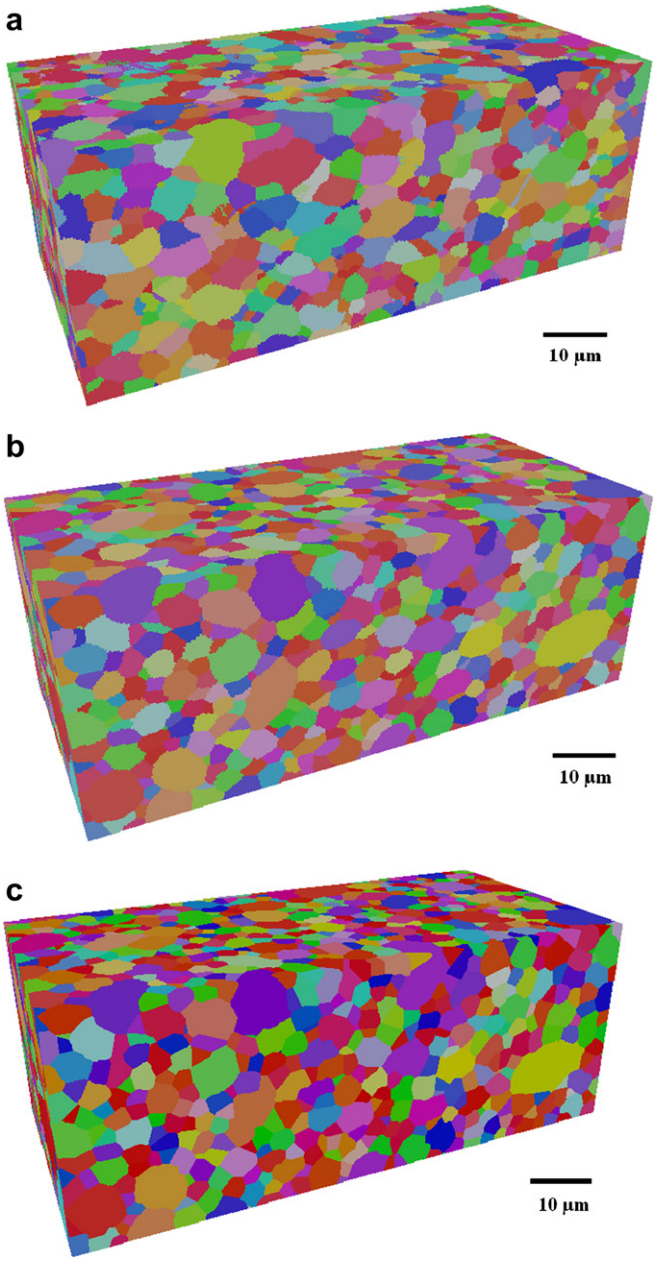

Fig. 2. (a) experimental volume from reconstructed EBSD maps as presented in Part 1 of this set, (b) synthetic volume containing 5269 grains created by the CGP module (modules A + B) and (c) same synthetic volume created after SPG-CVTT module (modules A − D). Each volume has dimensions 96 μm × 36 μm × 46 μm. Note that each color refers to a crystallographic orientation and the grains in (b) have been assigned the same colors as the corresponding grain in (c) since orientations are not assigned during the generation process until module D.

mal distribution of grain size observed for IN100. Finally, the localized nature of non-uniform distributions in size and shape of grains are virtually impossible to recreate using random Voronoi tessellations. Consequently, the CVTM is developed to improve the statistics of the traditional Voronoi tessellation method. Fig. 3 illustrates the process of biased seed point generation in the CVTM using the following steps:

(i) The centroids of the non-ellipsoidal grains, obtained from the output of the CGP module, are evaluated from a voxelized representation using the relation:

$$x_c = \frac{I_x}{I_0}, \quad y_c = \frac{I_y}{I_0}, \quad z_c = \frac{I_z}{I_0}, \tag{9}$$

where I_x, I_y and I_z are the first-order moments of the voxelized grain and I_0 is the zero-order moment. This is shown in Fig. 3a.

(ii) The representative volume is now tessellated into a network of Voronoi cells, as shown in Fig. 3b, using these centroids. Fig. 3b clearly illustrates that there is a significant difference between the original grain structure and the result of the Voronoi tessellation. To compensate for this difference and represent the grains more accurately, additional seed points are inserted. The principal idea behind this seed addition process is to retain the spatial position of the interface between two grains.

(iii) The location of each additional seed point is guided by the position of the interface between two voxelized grains produced by the CGP module with respect to the grain centroids shown in Fig. 3a. To represent the grain boundary between two grains, its centroid is calculated using Eq. (9). For the purpose of boundary centroid evaluation, the interface is represented as a thin layer with thickness equal to the voxel size. The boundary centroid need not lie on the boundary itself, just as the centroid of a concave object need not lie within the object's volume.

Since the Voronoi cell boundary is represented as the perpendicular bisector of the line joining two seed points, the additional seed point should be placed in the larger of the two grains and at a position from the grain boundary equal to the distance from the smaller grain's centroid to the grain boundary. This placement will result in the

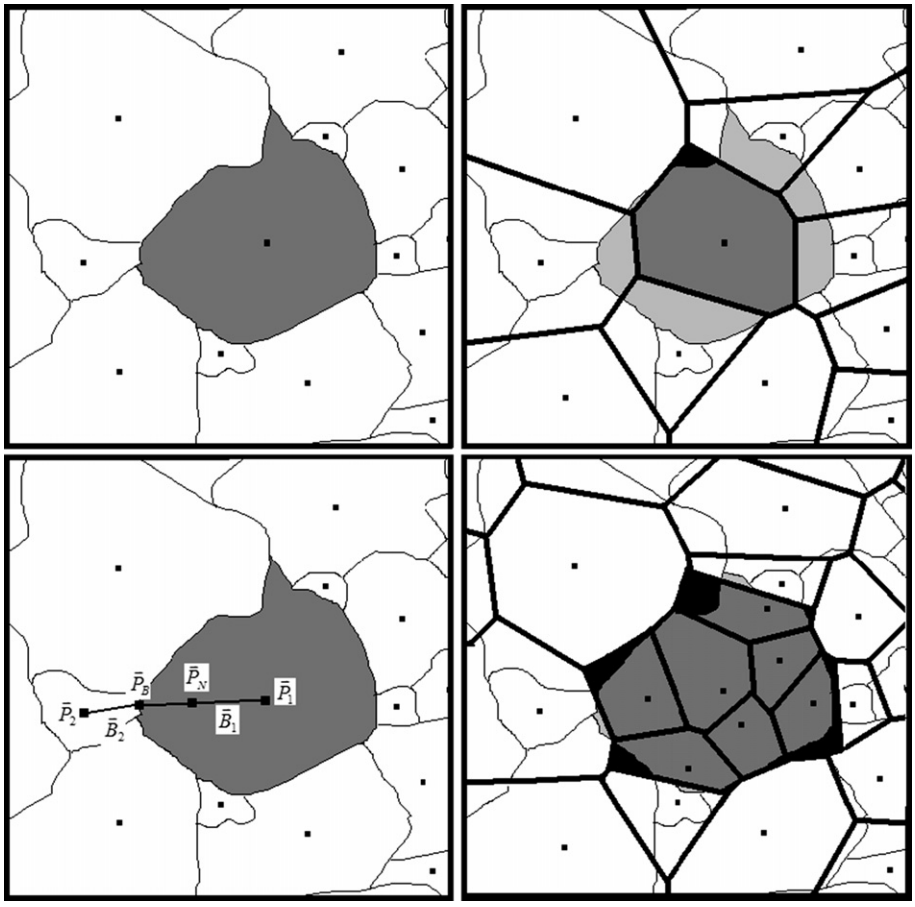

Fig. 3. Schematic of seed point generation: (a) example microstructure, (b) grain approximated by single Voronoi cell using centroid, (c) creation of an additional seed points and (d) grain approximated by multiple Voronoi cells merged together. Only one grain (dark gray) is modeled in this schematic for illustration purposes and is not necessarily representative of the process when all grains are modeled. Note that the area of the grain missed by Voronoi cells is shaded light gray and overextended areas are shaded black.

perpendicular bisector of these two seed points passing through the grain boundary centroid, effectively representing the boundary as a plane. In order to determine the position of the additional seed point, the centroids of the grains (P_1 and P_2) that share the boundary are connected to the boundary centroid P_B and the respective distances are calculated. The new seed point P_N is placed along the larger of the lines $\vec{P_i}\,\vec{P_B}$ $(i = 1, 2)$ at a position given by

$$\vec{P_N} = \vec{P_i} + \left(1 - \frac{\delta_j}{\delta_i}\right)(\vec{P_i} - \vec{P_B}) \quad \text{for } \delta_i > \delta_j \ (i, j = 1, 2), \tag{10}$$

where $\delta_1 = |\vec{P_1} - \vec{P_B}|$ and $\delta_2 = |\vec{P_2} - \vec{P_B}|$. Fig. 3c shows a 2D schematic of the process of point generation and Fig. 3d shows the result of the Voronoi tessellation with the additional seed points. The Voronoi cell generated as a consequence of this point addition belongs to parent grain.

The number of additional seed points can be controlled to optimize accuracy of the representation and computational efficiency. The criterion in Eq. (10), $\delta_i > \delta_j$ $(i,j = 1,2)$, can be changed to $\delta_i > \alpha\delta_j$ $(i,j = 1,2)$, where α is a user-defined variable greater than 1. When $\alpha = 1$, every boundary will produce an additional seed point (provided the two grain centroids are not exactly equidistant from the boundary centroid). As α is increased, boundaries that are only slightly closer to one grain centroid (i.e. $\frac{\delta_i}{\delta_j} < \alpha$ $(i, j = 1, 2)$) will not produce an additional seed point. At the extreme, as $\alpha \to \infty$, no boundary will produce an additional seed point and only the centroids will be used in the tessellation. The sensitivity of the Voronoi representation's accuracy with respect to the number of seed points used is shown in Fig. 5 and will be discussed in Section 3.

Subsequent to the additional seed point generation procedure (SPG), the CVTT module invokes a Voronoi tessellation program [12–14] to create a network of Voronoi cells from these seed points. This Voronoi cell-based grain structure representation is further modified to eliminate small edges and faces that can have adverse impact on a finite-element (FE) mesh generation procedure. The SPG-CVTT module allows the user to define a minimum edge length, and edges shorter than the tolerance are collapsed. This modification procedure is necessary in the preparation of these structures for mesh generation, but is beyond the scope of this paper. The effects and sensitivities of this process are the subject of a more detailed investigation of mesh generation and the topic of a later paper.

Finally, Voronoi cells belonging to the same grain, as determined by a grain ID number assigned to each seed point, are merged. All faces shared between these cells are referred to as "internal faces" because they are within the bulk of the grain, not on the grain surface. The internal faces are removed by discarding any face that belongs to more than one of the cells. After this process only the faces that lie on the outside of the aggregate of Voronoi cells, corresponding to the grain boundary, remain. The Voronoi cell construct generally extends to infinity and should be bounded to be within the domain of the representative volume. To enable this process, each grain is intersected with the six planes of the bounding volume. The representative polycrystalline volume resulting from the SPG-CVTT module is shown in Fig. 2c and the corresponding comparison with the experimental statistics is shown in Fig. 4. A statistical comparison between the Voronoi-based representative volume (at varying values of α) and the voxelized representative volume is shown in Fig. 5 and will be discussed in Section 3.

2.4. Module D: Crystallographic orientation assignment (COA)

The experimental observations in Part 1 did not reveal a strong correlation between the crystallographic and morphological characteristics of the IN100 microstructure. Consequently, the crystallographic orientation assignment in this paper is assumed to be uncorrelated with the morphological grain construction and will be performed independently. The COA module assigns crystallographic orientations to the grains, such that the orientation and misorientation distribution functions (ODF and MoDF) as well as the microtexture function (MTF) are statistically equivalent to the experimental dataset. The process of the orientation probability assignment method (OPAM), misorientation probability assignment method (MPAM) and microtexture probability assignment method (MTPAM) have been discussed in an earlier paper [15]. A summary of these methods is provided in the following sections.

2.4.1. Orientation probability assignment method (OPAM)

The orientation probability assignment method is similar to the shape orientation assignment discussed in module A. The difference is that the set of rotations, expressed as Euler angles (ϕ_1, Φ, ϕ_2), now transform the global coordinates onto the crystallographic axes of the grain, rather than the principal axes of the ellipsoid. If $N^{(i)}$ is the number of points in the ith crystallographic orientation space element ranging from $(\varphi_1, \Phi, \varphi_2)$ and $(\varphi_1 + \Delta\varphi_1, \Phi + \Delta\Phi, \varphi_2 + \Delta\varphi_2)$, then the density of orientations can be expressed as $\frac{N^{(i)}}{N}$. To evaluate this density, the entire crystallographic orientation space is defined as a finite cube with edge length π (90°) with the origin at one of its vertices. For the purpose of creating ranges in the orientation data, the orientation space is discretized into cubic bins of dimension $\pi/36$ or 5°. The crystallographic orientation density in each bin is calculated by dividing the number of orientations in the bin by the total number of orientations in the experimental data. Crystallographic orientations are created and assigned based on this probability density function. The orientation distribution generated is thus statistically equivalent to the experimental dataset.

2.4.2. Misorientation probability assignment method (MPAM)

Randomly assigning the orientations does not ensure that the local pairing of orientations is correct. In order

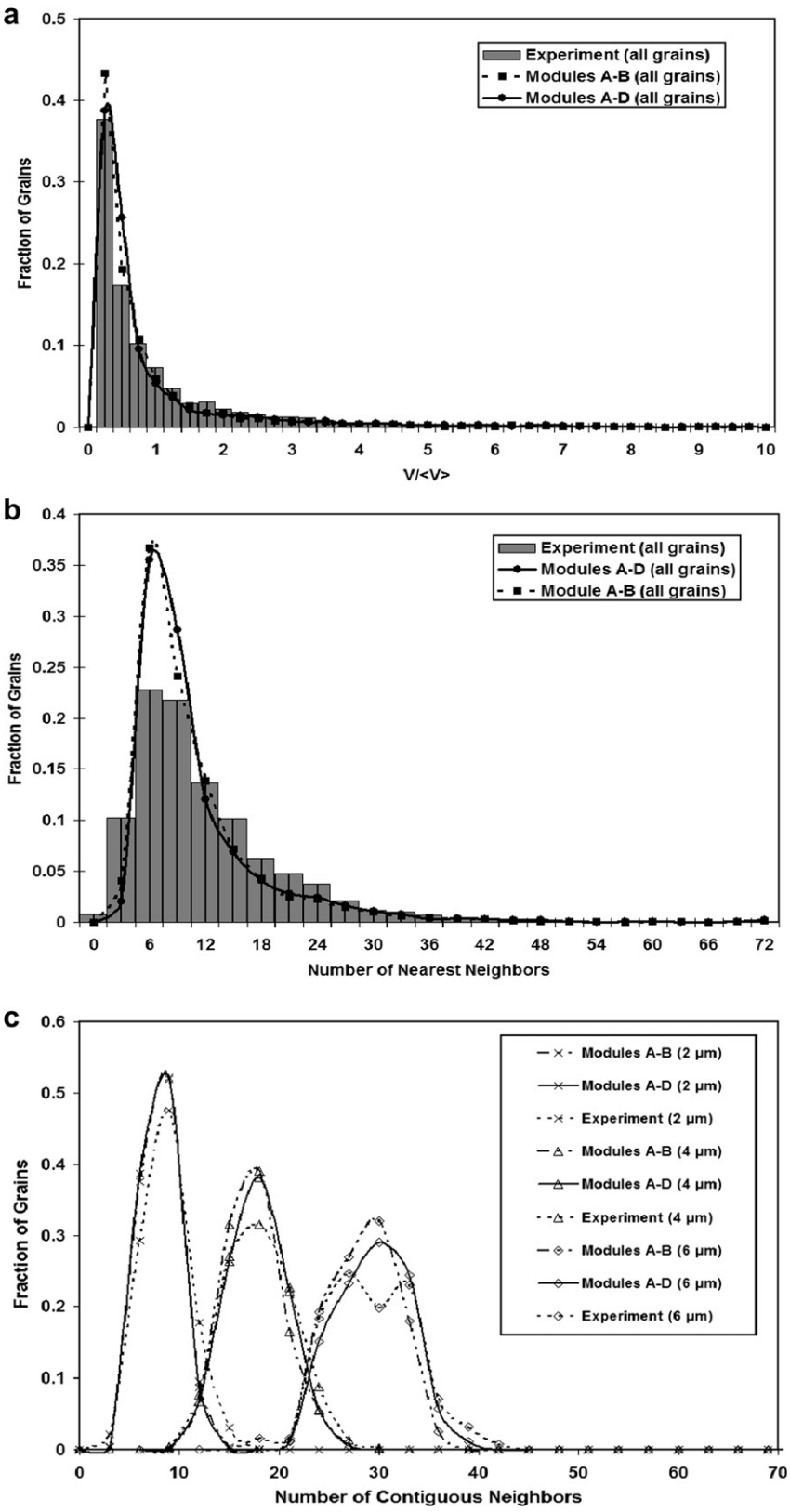

Fig. 4. Comparison of: (a) normalized grain volume, (b) number of neighbors, (c) number of neighbors–grain size correlation, (d) neighbor grain size–grain size correlation, (e) *b*/*a*-grain size correlation and (f) MoDF for experimental and simulated microstructures at various stages.

to quantify neighboring orientation pairs, the misorientation distribution function (MoDF) is used. Details of the definition and calculation procedure of misorientation are discussed in [16]. Misorientation is described in terms of a rotation axis vector **n**, which represents a common axis for both crystal lattices, and an angle θ, which is the

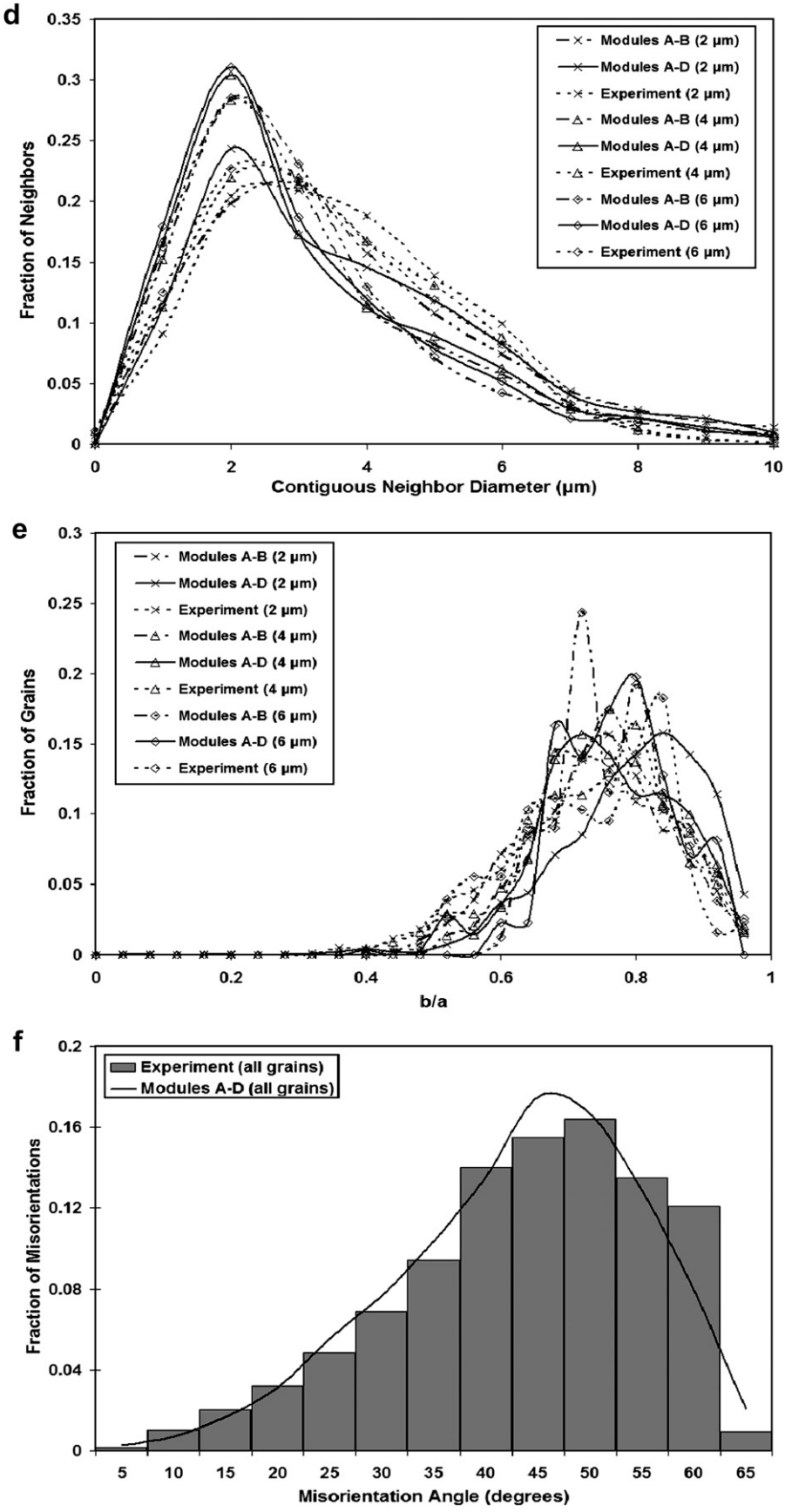

Fig. 4 (*continued*)

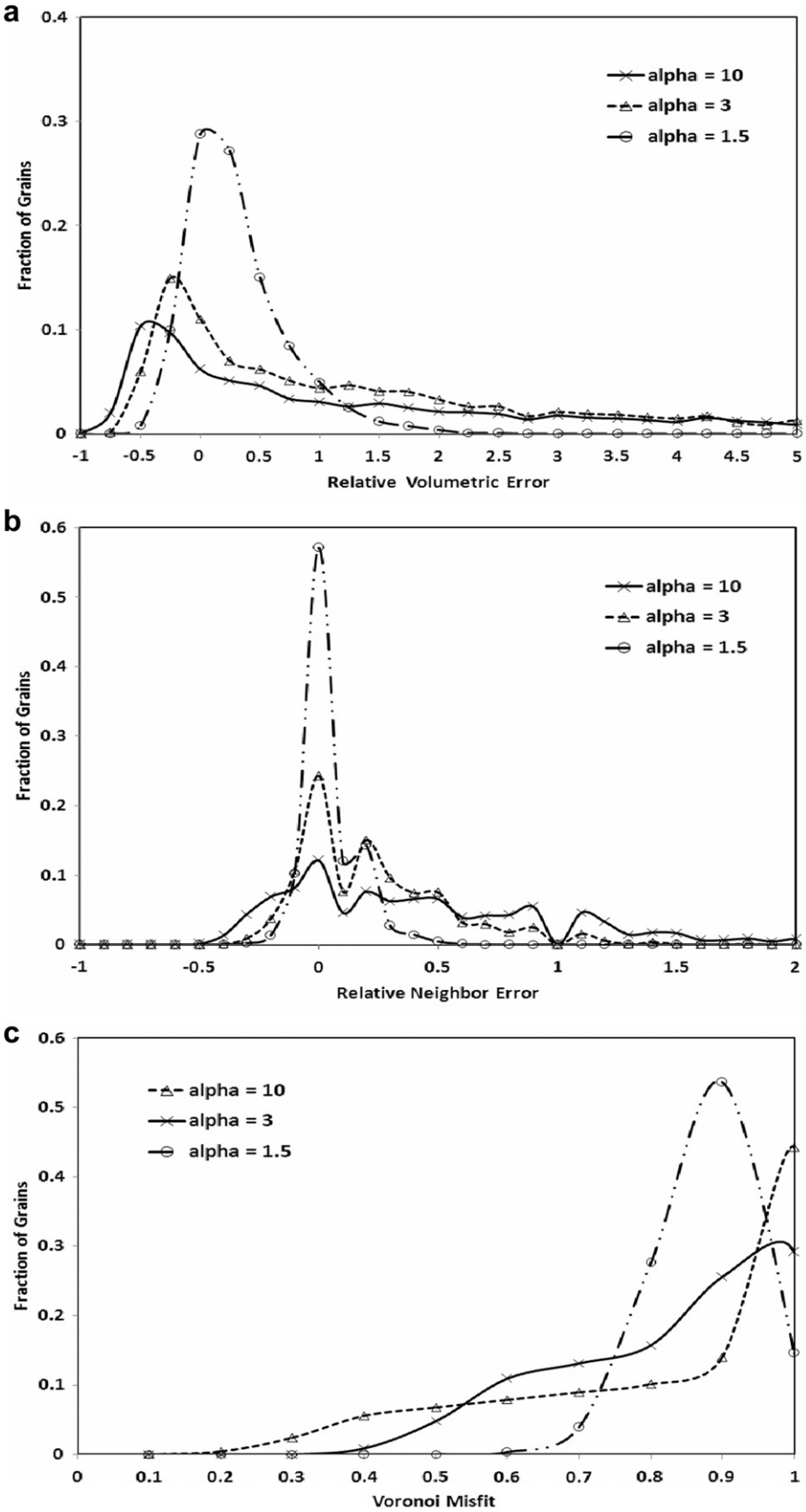

Fig. 5. Amount of error between voxel-based and Voronoi-based representations for different values of α: (a) relative volumetric error $(\frac{V_{\text{Voronoi}}-V_{\text{voxel}}}{V_{\text{voxel}}})$, (b) relative neighbor error $(\frac{NN_{\text{Voronoi}}-NN_{\text{voxel}}}{NN_{\text{voxel}}})$, and (c) Voronoi misfit $(\frac{\#\text{of voxels inside}}{\#\text{of voxels total}})$. As α is decreased the amount of error between the voxel-based and Voronoi-based representations also decreases.

rotation about **n** needed to bring the two crystal lattices into coincidence. This definition is same as the disorientation value calculated by commercial EBSD software and is given by

$$\theta = \min \left| \cos^{-1} \left\{ \frac{\mathrm{tr}(g_B g_A^{-1} O) - 1}{2} \right\} \right|, \tag{11}$$

where g_A and g_B are the orientation matrices of grains A and B, respectively and O is the crystal symmetry operator. The following steps are executed in the misorientation probability assignment method (MPAM):

(i) A set of 13 misorientation bins is created for misorientation angles between 0° and 65°. Each bin in this set has an angle increment of 5°.
(ii) The experimental data of misorientation angles between immediate neighboring grains is recorded. The number of simulated grain-pairs, for which the misorientation angle is within each of the 5° angular increments, is recorded.
(iii) The 13 statistical bins are rank-ordered based on the difference in their number fraction values between the experimental and simulated misorientation distributions. The bin with the largest difference value is assigned the greatest rank. The rank is also given a sign to signify whether it is in excess or deficit over the experimental bin. The excessive bins receive a positive sign and while the deficient bins are ranked with a negative value.
(iv) Each grain (or orientation) is ranked by summing the ranks of the bins to which each of the grain's misorientations belong. The grain ranking scheme is given by

$$R_i^G = \sum_{j=1}^{N} R^B(M_{ij}), \tag{12}$$

where R_i^G is the rank of grain i, $R^B(M_{ij})$ is the rank of the bin to which misorientation M_{ij} belongs, M_{ij} is the misorientation between grain i and grain j and N is the number of neighbors of grain i.
(v) Orientations belonging to grains with the highest ranks are selected for relocation. One distinct advantage of this technique relative to a traditional Monte Carlo process is that the relocation process is not completely random, but has a favorable bias.

2.4.3. Microtexture probability assignment method (MTPAM)

The final step in the COA module is to match the local clustering of similarly orientated grains. The MoDF begins to quantify local neighborhoods, but does not capture clustering of orientations because it does not relate relative spatial locations of the misorientations. In order to measure the amount of clustering the MTF is incorporated to the COA module. The MTF is defined in this work by the distribution of the fraction of a grain's neighbors having low misorientation (<15°). A value of zero corresponds to a grain with no similarly oriented neighbors and a grain with a value of one shares low misorientation with all of its neighbors. Clearly, high values in the MTF correspond to grains inside of local clusters of similarly oriented grains. The following steps are executed in the microtexture probability assignment method (MTPAM):

(i) A set of 4 statistical bins is set-up for number fraction of grains that have low misorientations with their neighbors (<15°). The bins are for the cases when: (a) none of the neighbors have a low misorientation, (b) between 0% and 33.33% of the neighbors have a low misorientation, (c) between 33.33% and 66.66% of neighbors have a low misorientation and (d) between 66.66% and all of the neighbors have a low misorientation.
(ii) Each grain i is assigned a value n_j corresponding to the number of its neighbors with which it shares low misorientation.
(iii) After the process of assigning values for each grain in the ensemble, each grain is ranked by summing the contribution it gives to each of its neighbors. This ranking is given by

$$R_i^G = \sum_{j=1}^{N} n_j \cdot H(M_{ij}), \tag{13}$$

where $H(M_{ij}) = 1$ for $M_{ij} > 15°$ and zero otherwise.
(iv) Grains that have the highest rankings are selected for relocation.

Having described the MTPAM, one should note that for the IN100 material investigated in Part 1, there was no apparent microtexture present. The combination of OPAM, MPAM and MTPAM creates a statistically equivalent crystallographic description in the synthetic, simulated microstructure.

3. Validation of simulated representative polycrystalline microstructures

In this section, the representative polycrystalline microstructures generated by the CGP module (modules A + B in Section 2) and the SPG-CVTT module (modules A − D in Section 2) are compared with the experimentally obtained microstructure to validate their statistical equivalence and accuracy. Additionally, the statistical differences between the two representative structures are also shown to highlight the benefits and limitations of the tessellation process. The microstructures from experiment and by the CGP and SPG-CVTT modules are shown in Fig. 2a–c, respectively. Visual comparison of Fig. 2b and c shows excellent agreement. However, these microstructures do not appear identical to Fig. 2a, which is expected since the simulated structures are intended to be statistically equivalent to the experimental structure but have different arrangements of the grain locations. As a result, each simulated structure should appear visually similar, not iden-

tical, and exhibit statistical equivalence. Fig. 4a–f compares the distributions of a number of microstructural statistical descriptors for the experimental volume, to the simulated microstructure by the CGP and SPG-CVTT modules, respectively. Table 2 lists the minimum, average and maximum values of selected statistical descriptors for the representative simulated microstructure after the CGP module and after the SPG-CVTT module have been executed.

Very close agreement is seen in the normalized grain volume distribution by all three methods in Fig. 4a. However, the maximum values of normalized grain volume for the simulated microstructures in Table 2 are significantly higher than that from experiments. It is quite probable that the choice of the log-normal representation of this parameter produces an outlier that is significantly larger than the experimental value. Also, the small size of the grain population acquired through the experiments is likely to limit the observation of some of the extreme values.

For each microstructure, the distribution of number of contiguous neighbors is displayed in Fig. 4b. While the general trend is in good agreement, the simulated microstructures show a difference in the density near the average value of the distribution. The distributions of the simulated volumes became more closely distributed about the average. A reason for this could be that the grain placement algorithm in module B forces grains towards average values of the number of neighbors in their respective grain volume bin. It is possible that an acceptance criterion to allow occasional low probability arrangements would aid in broadening these distributions. The same trend is also seen in Fig. 4c, which illustrates the correlation between number of neighbors and the grain size. In each grain size bin, the distribution of number of neighbors is centered about the same average value, but exhibits a tighter distribution. The three peaks in Fig. 4c correspond to the distributions of three grain size bins and clearly illustrate the correlation between the number of contiguous neighbors and grain size. The difference in the maximum value of number of neighbors between the experimental and simulated microstructures is also seen in Table 2 and may be directly linked to the larger maximum grain size in the simulated structures.

Fig. 4d shows the distribution of neighbor grain sizes for different grain sizes. The figure shows distributions for the same three grain size bins shown in Fig. 4c. Clearly, the similarity of the distributions for the different grain sizes infers that there is not a strong correlation between the neighbor grain size and grain size. However, in comparison with the experimental distributions, the distributions of the simulated microstructures shift towards smaller neighbor sizes. This corresponds to a larger fraction of small neighbors for each grain. The probable cause of the shift is the sequence of ellipsoid placement, during which the largest grains are placed first and are thus less likely to neighbor each other. The smaller grains fit into the regions between previously placed grains more easily, leading to a slight increase in the probability of having a small grain as a neighbor.

Fig. 4e illustrates the distributions of grain shape, represented by aspect ratios (b/a and c/a) of the ellipsoidal grains, which shows that the aspect ratios are not correlated with grain size. The distributions of b/a for the simulated structures deviate more from the experimental distributions at lower values of b/a. This probably is a result of the pseudo-grain coarsening process. This process, used to allocate the unassigned volume, is likely to result in more equiaxed grains. Voxel allocation in the coarsening process is based on a criterion that attempts to minimize the surface area of the simulated grains. This criterion is also seen to affect the surface-to-volume ratio parameter listed in Table 2, where the simulated grains tend to have slightly lower value of surface-to-volume ratio since the simulated grains are more equiaxed.

Finally, the misorientation distribution (MoDF) is plotted in Fig. 4f with good concurrence. All of these results validate the effectiveness of the SPG-CVTT module in producing high quality statistically induced realistic instantiation (SIRI) of polycrystalline microstructures.

Fig. 5a–c shows three metrics for quantifying the error between the voxel-based and Voronoi-based representations. In each of the three figures the error metric is displayed as a function of the value of α. The value of α and its affect on the number of seed points used in the Voronoi tessellation are discussed in Section 2.3. Fig. 5a shows the relative volumetric error between the two representations. The relative volumetric error is given by $\frac{V_{\text{Voronoi}}-V_{\text{voxel}}}{V_{\text{voxel}}}$. It is clear from the tightening of the curve about low values of error that decreasing the value of α decreases the amount of relative volumetric error. This same trend is seen in the plot of relative neighbor error in Fig. 2b. The relative neighbor error is given by $\frac{NN_{\text{Voronoi}}-NN_{\text{voxel}}}{NN_{\text{voxel}}}$, where NN is the number of neighbors of a grain. Finally, Fig. 5c shows an error metric called the Voronoi misfit. The Voronoi misfit is similar in nature to the ellipsoidal misfit presented in the first part of this paper. For each grain, the Voronoi rep-

Table 2
List of statistical descriptors measured at various stages of representative volume generation process

Descriptor	Experiment			CGP module (A + B)			SPG-CVTT module (A − D)		
	Min	Avg	Max	Min	Avg	Max	Min	Avg	Max
Normalized volume	0.01	1.00	22.55	0.04	1.00	58.88	0.05	1.00	54.33
Number of neighbors	2.00	12.69	69.00	4.00	11.89	100.00	4.00	12.15	105.00
b/a	0.17	0.74	1.00	0.34	0.76	0.99	0.07	0.79	0.99
c/a	0.10	0.55	0.93	0.25	0.58	0.91	0.06	0.67	0.93
Surface-to-volume ratio	0.17	0.56	1.00	0.09	0.51	0.98	N/A	N/A	N/A

resentation is superposed on the voxel representation and the fraction of voxels that lie within the Voronoi representation is calculated as the Voronoi misfit. A value of one corresponds to a Voronoi representation that contains the entire voxelized grain (and possibly portions of other grains). Lower values of Voronoi misfit correspond to voxelized grains that lie with more significant portions outside of the Voronoi representation and thus larger errors. In Fig. 5c, it is again obvious that decreasing the value of α, which increases the number of seed points, reduces the error between the two representations.

The error metrics show that the Voronoi representation converges towards the voxel-based representation as the value of α decreases. The computational time required for creating the tessellation is not highly sensitive to the value of α and in turn the number of seed points. The computational time for $\alpha = 1$ is only about 6 h for a volume of the size discussed here. The major benefits of the Voronoi representation are a vastly reduced number of elements in comparison to the voxel-based representation and the "smooth" boundaries in the Voronoi representation. The voxel-based representation is significantly limited by the number of voxels and the "stair-stepped" nature of the grain boundaries. The Voronoi representation is not perfect and does still exhibit some sharp edges and can have a large number of elements when α is set very low. However, the tessellation process does create a relatively accurate and computationally more efficient representation of the grain structure.

4. Conclusions

In the materials modeling community today, there is need for robust microstructure builders and simulators that can be used in high-fidelity models for prediction of microstructure–property relations. The present study comprises a comprehensive effort, combining experiments, image analysis and characterization with computational geometry-based algorithms, to advance the state-of-the-art in this field.

The second of this two-part paper describes assembling a sequence of modules for microstructure simulation, including: equivalent ellipsoidal grain generator, constrained grain packer, seed point generator, constrained Voronoi tessellation tool and crystallographic orientation assignment. The collection of these modules and the experimental characterization processes comprise an automated methodology for simulating representative polycrystalline microstructures.

The results of the validation studies show that statistical equivalence is achieved by this tool for most of the critical morphological and crystallographic parameters. The statistical equivalence is also established at different stages of the overall generation process. For example, the CGP module alone can be used to produce voxelized microstructures that are statistically equivalent to the experimental observations. As a result, the user can choose to employ parametric grain boundary representation techniques [10,11] or the constrained Voronoi tessellation method (CVTM) after the CGP module generation process. The CVTM is seen to converge towards the voxel-based representation as the value of α is decreased, with little affect on the computational time required. This flexibility is vital in the effort to model material properties that may require differing levels of sophistication and fidelity in the microstructure representation.

In conclusion, this study is one of the first attempts to create a fully automated process that collects 3D microstructural information via serial-sectioning, provide quantitative measurements of property-controlling microstructural features and generate realistic statistically equivalent structures for modeling. The output of this synthetic microstructure generator can be easily interfaced with sophisticated finite-element (FE) mesh generators [11] and hence serve as a preprocessor to a FE model.

The development of the tools presented in this paper prompts an important discussion regarding the "representative nature" of any volume, experimental or simulated. The volumes created by this process are statistically equivalent in the context of a selected subset of descriptors to some level of convergence. Simulation studies, which are the topic of ongoing focus, will ultimately conclude the true functional equivalence of the experimental and simulated volumes from this study. It is the assertion of the authors that the "representative nature" of these volumes will certainly depend on the properties investigated. Currently, the authors postulate that the experimental and simulated volumes will yield equivalent simulations for any property governed by the statistical descriptors matched in the two structures. However, there are certainly many more statistical descriptors unmatched and many properties controlled by those unhandled descriptors. The utility of these tools, in their current state, is that a representative volume element (RVE) can be produced synthetically provided the property governing features can be identified and quantified.

References

[1] Ballani F, Daley DJ, Stoyan D. Comput Mater Sci 2006;35:399–407.
[2] Stroeven M, Stroeven P. Acta Stereol 1996;15:247–52.
[3] Barton NR, Dawson PR. Modell Simul Mater Sci Eng 2001;9:433–63.
[4] Coster M, Arnould X, Chermant JL, El Moataz A, Chartier T. Image Anal Stereol 2005;24:105–16.
[5] Kumar S. Ph.D. Thesis, Penn. State University, 1992.
[6] Tikare V, Cawley JD. Acta Mater 1998;46:1333–42.
[7] Saylor DM, Fridy J, El-Dasher BS, Jung KY, Rollett AD. Metall Trans A 2004;35A:1969–79.
[8] Russ JC, DeHoff RT. Practical stereology. 2nd ed. Kluwer/Plenum; 2000.
[9] DeHoff RT. J Microsc 1983;131:259–63.
[10] Bhandari Y, Groeber M, Ghosh S. CAD 2007. doi:10.1016/j.cad.2007.11.003.
[11] Bhandari Y, Sarkar S, Groeber M, Uchic MD, Dimiduk DM, Ghosh S. Comput Mater Sci 2007;41:222–35.
[12] Okabe A, Boots B, Sugihara K, Chiu SN. Spatial tessellations: concepts and applications of Voronoi diagrams. 2nd ed. Wiley; 2000.
[13] Wakai F, Enomoto N, Ogawa H. Acta Mater 2000;48:1297–311.
[14] Preparata FR, Shamos MI. Computational geometry: an introduction. 1st ed. Springer-Verlag; 1985.
[15] Deka D, Joseph DS, Ghosh S, Mills MJ. Metall Trans A 2006;37A:1371–88.
[16] Xie CL, Ghosh S, Groeber M. J Eng Mater Technol 2004;126:339–52.